Eur. Phys. J. A **18**, 75–86 (2003)
DOI 10.1140/epja/i2003-10047-9

THE EUROPEAN PHYSICAL JOURNAL A

Charge density: A probe for the nuclear interaction in microscopic transport models

E. Galichet[1,2,a], F. Gulminelli[3], D.C.R. Guinet[4], M.F. Rivet[1], J.F. Lecolley[3], R. Bougault[3], G. Auger[5], B. Borderie[1], B. Bouriquet[5], A. Buta[3], J.L. Charvet[6], A. Chbihi[5], J. Colin[3], D. Cussol[3], R. Dayras[6], D. Durand[3], J.D. Frankland[5], B. Guiot[5], S. Hudan[5], P. Lautesse[4], F. Lavaud[1], N. Le Neindre[5,b], O. Lopez[3], L. Manduci[3], J. Marie[3], L. Nalpas[6], J. Normand[3], M. Pârlog[1,7], P. Pawłowski[1], E. Plagnol[1], E. Rosato[8], J.C. Steckmeyer[3], B. Tamain[3], A. Van Lauwe[3], E. Vient[3], C. Volant[6], J.P. Wieleczko[5], and INDRA Collaboration

[1] Institut de Physique Nucléaire, IN2P3-CNRS, F-91406 Orsay cedex, France
[2] Conservatoire National des Arts et Métiers, F-75141 Paris cedex 03, France
[3] LPC Caen (IN2P3-CNRS/ENSICAEN et Université), F-14050 Caen cedex, France.
[4] Institut de Physique Nucléaire, IN2P3-CNRS et Université, F-69622 Villeurbanne cedex, France
[5] GANIL, CEA et IN2P3-CNRS, B.P. 5027, F-14076 Caen cedex, France
[6] DAPNIA/SPhN, CEA/Saclay, F-91191 Gif-sur-Yvette, France
[7] National Institute for Physics and Nuclear Engineering, RO-76900 Bucharest-Măgurele, Romania
[8] Dipartimento di Scienze Fisiche e Sezione INFN, Università di Napoli "Federico II", I-80126 Napoli, Italy

Received: 21 January 2003 /
Published online: 5 August 2003 –
Communicated by A. Molinari

Abstract. The transport properties of the $^{36}\mathrm{Ar} + {}^{58}\mathrm{Ni}$ system at $95\,\mathrm{A}\cdot\mathrm{MeV}$ measured with the INDRA array, are studied within the BNV kinetic equation. A general protocol of comparison between the N-body experimental fragment information and the one-body distribution function is developed using global variables, with a special focus on charge density. This procedure avoids any definition of sources and any use of an afterburner in the simulation. We shall discuss the feasibility of such an approach and the distortions induced by the finite detection efficiency and the completeness requirements of the data selection. The sensitivity of the different global observables to the macroscopic parameters of the effective nuclear interaction will be studied in detail.

PACS. 25.70.-z Low and intermediate energy heavy-ion reactions – 24.10.-i Nuclear reaction models and methods

1 Introduction

The study of reaction mechanisms in heavy-ion collisions has much advanced recently with the construction of 4π detectors, like INDRA, which have high geometrical efficiency, good granularity and low-energy detection thresholds. Thanks to these detectors, the formation and the decay of excited nuclei, created in nucleus-nucleus collisions at intermediate bombarding energies ($10\,\mathrm{A}\cdot\mathrm{MeV} < E < 100\,\mathrm{A}\cdot\mathrm{MeV}$) can be more thoroughly investigated. In this energy regime, it is now experimentally well established that the collisions are dominated by binary dissipative processes [1–4]. In such reactions a quasi-projectile and a quasi-target are formed and their excitation energy increases with decreasing impact parameter. At variance with the phenomenology of deep inelastic reactions at lower energy ($\approx 10\,\mathrm{A}\cdot\mathrm{MeV}$) [5,6] an important fraction of the observed particles and light fragments originate from a rapidity region intermediate between the quasi-projectile and the quasi-target [7–10]. The physical origin of this mid-rapidity emission is most probably a complicated and highly non-equilibrated interplay between mean field and N-N collisions [11,12].

To better understand the physics underlying binary dissipative processes (energy dissipation between the quasi-projectile and the quasi-target, mid-rapidity emission, ...), we must find experimental observables which can be directly associated with the nuclear interaction, *i.e.* are settled in the first steps of a collision.

[a] e-mail: galichet@ipno.in2p3.fr
[b] *Permanent address*: Institut de Physique Nuclaire, IN2P3-CNRS, F-91406 Orsay cedex, France.

These observables have to be confronted with dynamical simulations of collisions, either transport models derived from semi-classical mean-field theory [13–15] or one of the different types of molecular dynamics [16–18]. The Boltzman-Nordheim-Vlasov model, which belongs to the first family, will be considered in this paper. Transport theories describe the time evolution of the one-body distribution function, $f(\mathbf{r}, \mathbf{p}, t)$, which gives information about the average properties of the colliding nuclear system. Conversely, the observables measured in an experiment concern the physical and measurable characteristics of all reaction products $(Z, E_{\rm kin}, \theta)$, which are N-body variables. Any comparison between experimental data and transport theories requires to make a choice between the one-body and the N-body frameworks. The method frequently employed in the literature consists in calculating N-body variables in the theory. For this purpose, the transport calculation is stopped at the "freeze-out time", namely when the nuclear dynamics is over. At this time, hot fragments (sources) are defined and their decay can be taken into account by means of an evaporation or multifragmentation code. To be valid this method needs a clearly defined freeze-out time, in the sense that the dynamical and thermodynamical time scales have to be well separated; this may not always be true, particularly when the important energy dissipation implies comparable time scales for dynamical emission and particle evaporation. In principle, a molecular dynamics description is more appealing, since it directly provides simulated events which can be analyzed exactly as the experimental events. However, the N-body correlations being implemented only at an approximate level, even these models systematically need the use of an afterburner at a definite freeze-out time and it is often difficult to know whether a deviation between model and data can be ascribed to the equation of state and the transport properties of nuclear matter or rather to the specific implementation of secondary decay.

The alternative method proposed in this paper consists in constructing one-body observables within data and in treating events in their globality. This method avoids any definition of "sources" and is independent of the choice of the freeze-out time. Global variables are one-body observables that condensate the experimental information and allow a more simple characterization of the events by a shape description. A new and powerful global variable has been recently introduced, the charge density [19]. This variable is invariant under clusterization, and therefore well suited for visualizing the collisions as a function of their violence, and for direct comparisons with models.

In this paper, we will study the $^{36}\mathrm{Ar} + {}^{58}\mathrm{Ni}$ system at $95\,\mathrm{A}\cdot\mathrm{MeV}$. Experimental results, collected with the 4π array INDRA will be compared with the predictions of Boltzman-Nordheim-Vlasov calculations (BNV) [13]. We will first discuss the different steps of the calculation. Then the experimental details and the event selection will be presented. The comparison between experimental and calculated observables will follow. A closer look at the physical origin of the mid-rapidity component will be given before the conclusion.

2 Theoretical model predictions

2.1 Presentation of BNV

The BNV code has been run for the $^{36}\mathrm{Ar} + {}^{58}\mathrm{Ni}$ system at $95\,\mathrm{A}\cdot\mathrm{MeV}$ for impact parameters ranging from $b = 1$ fm to $b = 10$ fm, above which only elastic scattering is observed. BNV is a numerical simulation of the semi-classical nuclear Boltzmann transport equation. In this approach one calculates the space-time evolution of the one-body distribution function under the influence of the mean field, the nucleon-nucleon collisions and the Pauli principle. The detailed description of the model and the method employed for computer simulations can be found in ref. [13].

In the present study the mean-field potential, $U_{\rm MF}$, is parameterized with a Skyrme interaction which reads

$$U_{\rm MF}(\rho_n, \rho_p) = A\rho + B\rho^n + C\nabla^2\rho + D(\rho_n - \rho_p)\tau_p + U_{\rm coul}(\rho_p)\,, \quad (1)$$

where ρ, ρ_n, ρ_p are respectively the nuclear, neutron and proton density and τ_p is the isospin of the concerned nucleus. The coefficients C, D are fixed to reproduce the surface and the symmetry terms of the liquid-drop energy; A, B and n are chosen to account for the properties of the saturation point of nuclear matter, binding energy, saturation density and compressibility. The incompressibility coefficient, $K = 220$ MeV, corresponds to a soft equation of state. The momentum dependence of the mean field is neglected.

The nucleon-nucleon elastic cross-section σ entering the collision integral is taken equal to the free cross-section $\sigma_{N\text{-}N}(E, \theta, \tau_z)$ with the experimentally measured dependences on energy, scattering angle and isospin [20]. The neglect of momentum dependence [14,21,22], in-medium effects on the nucleon-nucleon cross-section [23–27] and higher-order terms in the symmetry energy [28] are drastic assumptions that will be checked from the comparison with data. If sizeable deviations from the predictions of the theory are observed, this will demonstrate the sensitivity of the observables to these fundamental properties of nuclear transport.

For a meaningful comparison of the results of the simulations with experimental data, the internal Fermi momentum component of $f(\mathbf{r}, \mathbf{p}, t)$ has to be deconvoluted from the translational motion using a coalescence procedure. This step is added at some asymptotic time, $t_{\rm clus}$, and from this time the long-range Coulomb interaction can be added up to infinity in an exact manner. The coalescence procedure thus in principle introduces an arbitrary time scale which is exactly what we want to avoid; the challenge will then be to show that some observables exist (namely global variables) that are independent of the choice of $t_{\rm clus}$ and can therefore be used for an unambiguous comparison with data. This step will be detailed in the next subsection.

2.2 Coalescence

The coalescence procedure is the same as described in ref. [29]: A test particles are randomly chosen among the $n_{\rm tot} = n_{\rm tp} \times A$ test particles, where A is the total mass of the system and $n_{\rm tp}$ is the number of test particles per nucleon. For this analysis $n_{\rm tp}$ is equal to 426. The proportions of neutrons and protons, and of projectile and target nucleons are conserved, as well as the total velocity. For every test particle we calculate a proximity criterion in position space:

$$\|\mathbf{r}_i - \mathbf{r}_j\| < d_{\rm coal} = C \left(\frac{1}{n_{\rm tp} \times \rho_0} \right)^{1/3} \qquad (2)$$

in order to form fragments at normal density, ρ_0 ($\rho_0 = 0.16$ nucleon/fm^3).

An additional proximity criterion in momentum space allows to roughly account for particle evaporation, to end up with cold fragments:

$$\|\mathbf{p}_i - \mathbf{p}_{\rm cm}\|^2 \leq p_{\rm F}^2 + 2mB_E \,, \qquad (3)$$

where $\mathbf{p}_{\rm cm}$ is the center-of-mass momentum of the fragment calculated with the proximity criterion in position space. $p_{\rm F}$ is the local Fermi momentum and B_E is an average binding energy, here taken as $B_E = 8$ MeV.

Coulomb correlations have been added on the fragments reconstructed from coalescence up to a time, where all observables are stable.

Note that the clusterization procedure produces a sample of events, leading to distributions of values of the variables for a given impact parameter. It thus restores some fluctuations around mean values which were lost in the transport calculation. It has been demonstrated in ref. [13] that the correlations built by the clusterization procedure reproduce the correct (low-amplitude) fluctuations at the one-body level. Global variables can now be built on these events just as in experimental data.

2.3 Analysis variables

As quoted above, we are interested in the global variables independent of the clusterization time. In the following we study the behavior of some among the many possible variables which are commonly used (see, for example, refs. [30, 31]) in the analysis of heavy-ion collisions. In figs. 1 and 2 are represented for different impact parameters the variation with $t_{\rm clus}$ of the predicted charged-particle multiplicity and the heaviest-fragment charge distributions. With increasing $t_{\rm clus}$, the average multiplicity increases and the charge of the heaviest fragment decreases. Two reasons can be invoked to explain this behavior. The first one is physical: indeed, when $t_{\rm clus}$ increases the hot fragments evaporate nucleons; consequently, the smaller time shown in the figures cannot yet be considered as asymptotic. (Recall that the p-space coalescence written in eq. (3) accounts only approximately for evaporation.) The second reason is inherent to BNV. Since the mean field cannot describe small fragments, the system will tend to vaporize in

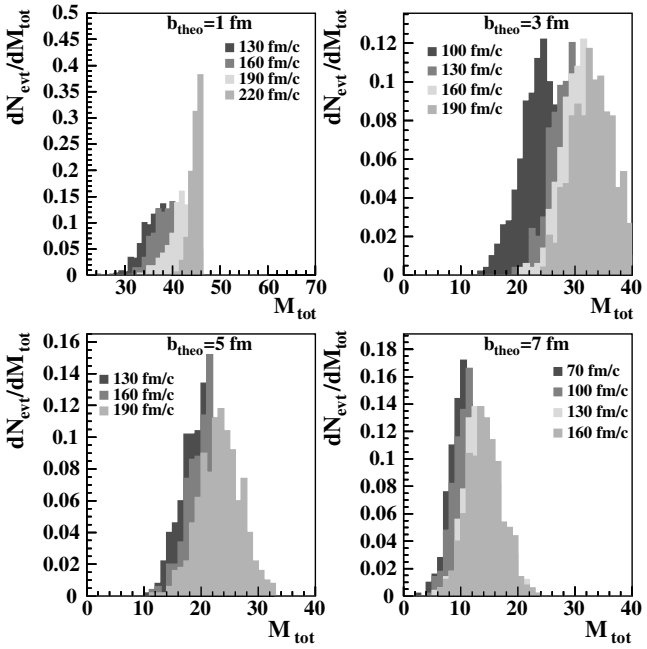

Fig. 1. Evolution of the calculated charged-particle multiplicity with $t_{\rm clus}$ (see text), for 95 A $\cdot$ MeV ^{36}Ar + ^{58}Ni collisions at different impact parameters ($b_{\rm theo} = 1, 3, 5, 7$ fm).

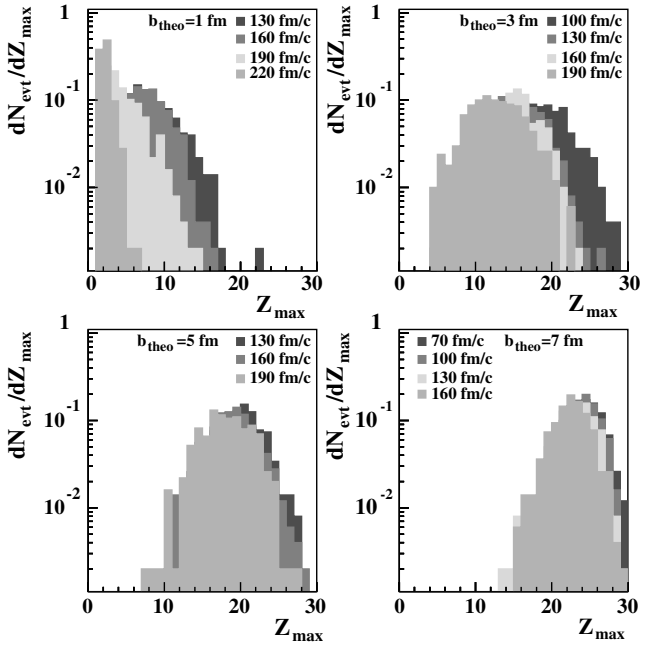

Fig. 2. Evolution of the calculated heaviest-fragment charge distributions with $t_{\rm clus}$ for 95 A $\cdot$ MeV ^{36}Ar + ^{58}Ni collisions at different impact parameters ($b_{\rm theo} = 1, 3, 5, 7$ fm).

free nucleons if the deposited energy is comparable to the binding energy. This is indeed observed for the most central collisions, showing that BNV predicts a non-realistic large complete vaporization cross-section of the system (see fig. 1, for $b = 1$ fm, the average multiplicity is equal to the total charge of the system). It is worth mentioning here that a small "vaporization" cross-section (500 μbarns) was

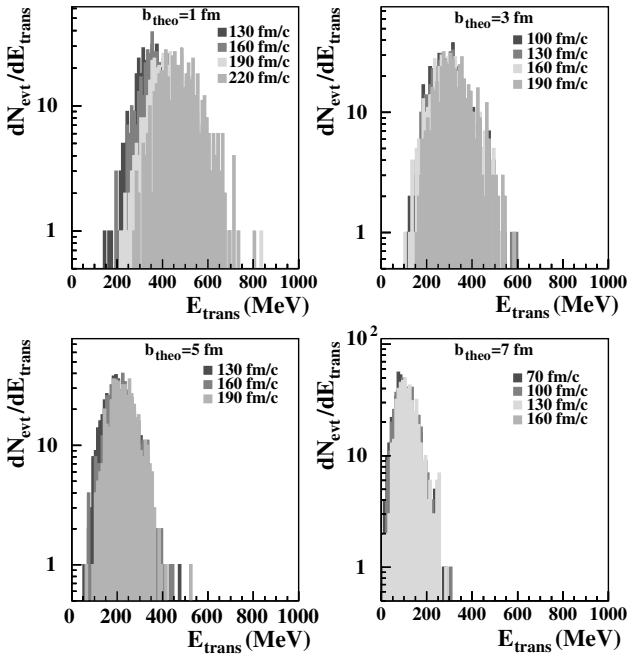

Fig. 3. Evolution of the calculated transverse-energy distribution with $t_{\rm clus}$ for 95 A $\cdot$ MeV ^{36}Ar + ^{58}Ni collisions at different impact parameters ($b_{\rm theo} = 1, 3, 5, 7$ fm).

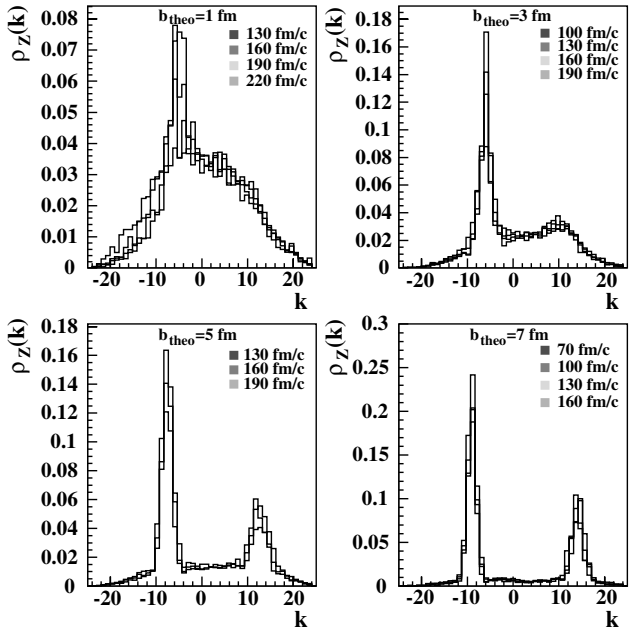

Fig. 4. Evolution of the calculated charge density, $\rho_z(k)$ with $t_{\rm clus}$ for 95 A $\cdot$ MeV ^{36}Ar + ^{58}Ni collisions at different impact parameters ($b_{\rm theo} = 1, 3, 5, 7$ fm). $k = V_{\rm cm}/10$.

observed experimentally [32,33]; the corresponding events comprise, however, not only nucleons but also helium and hydrogen isotopes, and the average total charged-particle multiplicity is equal to 29. In conclusion, neither the multiplicity distribution nor the charge of the heaviest residue match the required criterion of invariance on $t_{\rm clus}$.

In figs. 3 and 4 we have represented two examples of global variables describing the event in momentum space. The total transverse energy, shown in fig. 3, presents essentially no dependence on $t_{\rm clus}$ for semi-central to peripheral impact parameters. A substantial ($\sim 35\%$) increase of the average value of $E_{\rm trans}$ when $t_{\rm clus}$ increases from 130 to 220 fm/c is only observed for very central collisions ($b = 1$ fm). This indicates that the asymptotic time is long for these collisions. The charge density, $\rho_z(k)$ presented in fig. 4, is another global variable connected with the shape of the event in momentum space [19,34,35]. The charge density is defined as the quantity of charge projected on the main axis of the ellipsoid (calculated from the momentum tensor) in the center-of-mass velocity space. In fig. 4 the velocity axis is expressed in units of the center-of-mass velocity, $V_{\rm cm}$, and divided in k bins of width $\Delta k = V_{\rm cm}/n$, n is an integer number. The charge density along the k axis is then given by

$$\rho_z(k) = \frac{\sum_i Z_i(k)}{\sum_{i=1}^{M_{\rm tot}} Z_i}\,, \tag{4}$$

where the sum in the numerator runs over all charges in bin k, whereas the denominator is the sum of all charges in the whole k-interval. For peripheral collisions, two bulks of charges located at the quasi-projectile (QP) and the quasi-target (QT) velocities are well separated; with increasing centrality a growing contribution of matter between the quasi-projectile and the quasi-target can be observed. The global shape of the charge density distributions does not evolve with $t_{\rm clus}$, in the sense that the quantities of charges at mid-rapidity and around the QP and QT velocities, as well as the positions of the latter, remain the same. This confirms the invariance under clusterization expected theoretically for $\rho_z(k)$ [19]. Evaporation modifies, however, each of the QP/QT peaks which become lower and broader with increasing $t_{\rm clus}$, up to an asymptotic time. For times longer than the longest time reported in fig. 4 the distributions do not change any more.

The same independence from $t_{\rm clus}$ is observed for other global variables [30], like the isotropy ratio $\left(R_p = \frac{2}{\pi}\frac{\sum_{i=1}^{M_{\rm tot}}|\mathbf{P}_{\rm per}|}{\sum_{i=1}^{M_{\rm tot}}|\mathbf{P}_{\rm par}|}\right)$, (where $\mathbf{P}_{\rm per}$ (respectively $\mathbf{P}_{\rm par}$) is the projection of the momentum of each particle perpendicular to (respectively along) the beam axis) or the flow angle ($\theta_{\rm flow}$), which is often used to select central collisions [36].

Owing to the observed evolution of the global variables discussed above, in the following the values of $t_{\rm clus}$ have been fixed to 220 fm/c for $b_{\rm theo} \leq 3$ fm, 190 fm/c for $b_{\rm theo} = 4$–6 fm and 130 fm/c for $b_{\rm theo} = 7$–9 fm.

2.4 Sensitivity of global-variable distributions to the parameters of the interaction

Our purpose is to study the nuclear equation of state and the in-medium modifications to the nucleon-nucleon cross-section through an experimental point of view. We have

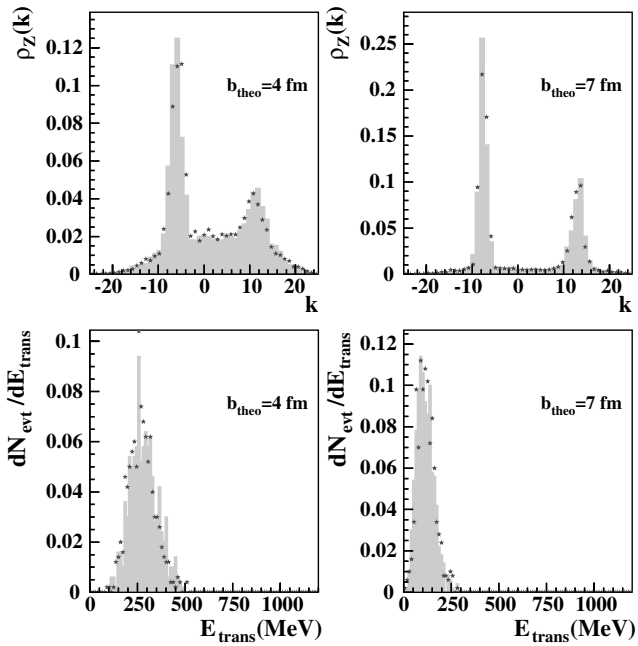

Fig. 5. Dependence on the incompressibility coefficient K of charge density (upper pictures) and transverse-energy (lower pictures) distributions for 95 A$\cdot$ MeV ^{36}Ar + ^{58}Ni collisions at $b_{\rm theo}$ = 4 and 7 fm. The grey histograms and the black stars correspond to K = 220 MeV and K = 380 MeV, respectively. $k = V_{\rm cm}/10$.

looked at the energy dissipation and the matter repartition during collisions through the evolution of two global observables. Firstly, the transverse energy, which is correlated to the dissipation; for the system studied here, the quasi-projectile and quasi-target velocities remain roughly parallel to the projectile direction; consequently the transverse energy essentially reflects the properties of mid-rapidity emissions. Secondly, the charge density distribution, which represents exactly the repartition of matter in a collision. So, in this subsection we will examine the sensitivity of these two global variables to the parameters of the interaction used in the model, the incompressibility coefficient and the nucleon-nucleon cross-section.

2.4.1 Influence of K

The incompressibility coefficient characterizes the mean field, which is described in BNV by a Skyrme interaction (eq. (1)). Most studies on giant monopole resonances and transverse flow presently agree on a soft equation of state $K \approx 220$ MeV. However, it is well known that the momentum dependence of the nuclear mean field can mock up an increased stiffness [14]. Therefore, a sensitivity of the observables to K would indicate the generic possibility of learning something about the mean field from the system under study. In fig. 5 is shown, for two representative impact parameters, the behavior of the charge density and transverse-energy distributions, for K = 220 MeV, which is the initial value used to build figs. 1-4, and a very stiff equation of state K = 380 MeV. The evolution of the charge density indicates that compressibility has a negligible influence on the mid-rapidity region, and only a small effect on the relative velocity between the quasi-projectile and the quasi-target, which decreases when K increases; this effect is only sizeable for small impact parameters. For $b_{\rm theo}$ = 4 fm, the relative velocity, which represents $\sim$ 70% of the initial value, shows a 10% decrease when K increases from 220 to 380 MeV. The transverse-energy distributions are independent of the stiffness of the EOS. This trend is systematically observed for all impact parameters. The relaxation of the incoming momentum being quite small for the light ^{36}Ar + ^{58}Ni at these relatively high incident energies [33], studies at lower energy and (or) with heavier systems would be necessary to enlighten mean-field effects from the relative velocity between the two spectator residues. These findings indicate also that the quantity of matter emitted at mid-rapidity and its energy are not strongly correlated with the mean-field part of the nuclear interaction.

2.4.2 Influence of $\sigma_{N\text{-}N}$

The nucleon-nucleon cross-section $\sigma_{N\text{-}N}$ governs the collision probability in the BNV collision integral. Many different theoretical studies [23–27] indicate that the collision probability should be influenced by the nuclear medium. A screening effect as well as an enhanced collision probability are possible depending on the different theories and on the density and the temperature of the medium. To explore the possibility of settling medium effects from mid-rapidity data we have schematically multiplied the value of the cross-section in the vacuum, $\sigma_{\rm free}$, by a constant. The charge density and transverse-energy distributions are represented in fig. 6, for two representative impact parameters and three values of $\sigma_{N\text{-}N}$: $\sigma_{N\text{-}N} = \sigma_{\rm free}$ (the one used above), $\sigma_{N\text{-}N} = 2\times\sigma_{\rm free}$ and $\sigma_{N\text{-}N} = 0.5\times\sigma_{\rm free}$. The effects of a variation of $\sigma_{N\text{-}N}$ are much more pronounced than those of the mean field. Indeed, the higher is the cross-section the larger is the contribution to mid-rapidity and the lower is the transparency (in charge density distributions transparency is revealed by narrow peaks at the quasi-projectile and quasi-target velocities for central collisions). The relative velocity between the quasi-projectile and the quasi-target does not change under a $\sigma_{N\text{-}N}$ variation. These two results are very clear especially for central and semi-central collisions. Consistently with the increase of the charge density, the transverse energy increases with $\sigma_{N\text{-}N}$ especially for central collisions. From a quantitative point of view the variation of the average transverse energy is about twice smaller than the variation of the quantity of particles at mid-rapidity in the charge density for $b_{\rm theo}$ = 3 fm. This means that an augmentation of $\sigma_{N\text{-}N}$ increases the emission probability of particles, while slightly decreasing the average kinetic energy per particle.

From the presented study of BNV simulated data we can conclude that for the ^{36}Ar + ^{58}Ni at 95 A$\cdot$ MeV mean-field and residual-interaction effects appear to be clearly disentangled. Among the restricted number of observables

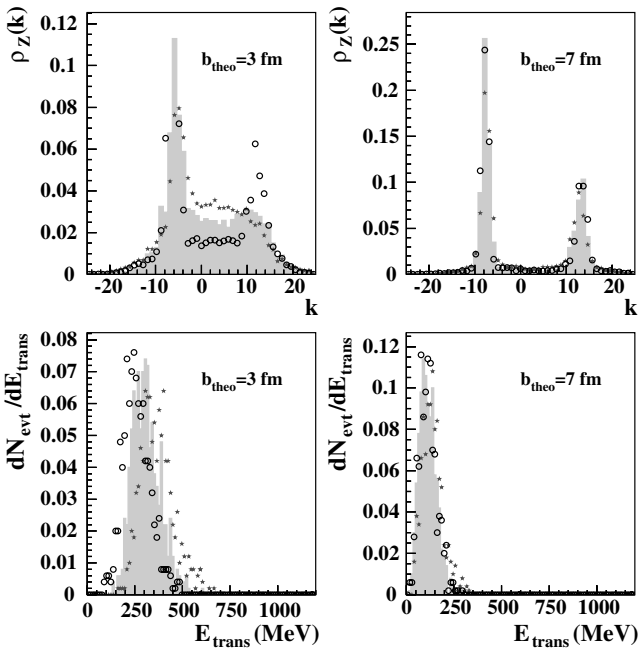

Fig. 6. Dependence on $\sigma_{N\text{-}N}$ of charge density (upper pictures) and transverse-energy (lower pictures) distributions for $95\,\mathrm{A}\cdot$ MeV $^{36}\mathrm{Ar} + {}^{58}\mathrm{Ni}$ collisions at $b_{\mathrm{theo}} = 3$ and 7 fm. The grey histograms correspond to $\sigma = \sigma_{\mathrm{free}}$, stars to $\sigma = 2 \times \sigma_{\mathrm{free}}$, and open points to $\sigma = 0.5 \times \sigma_{\mathrm{free}}$. $k = V_{\mathrm{cm}}/10$.

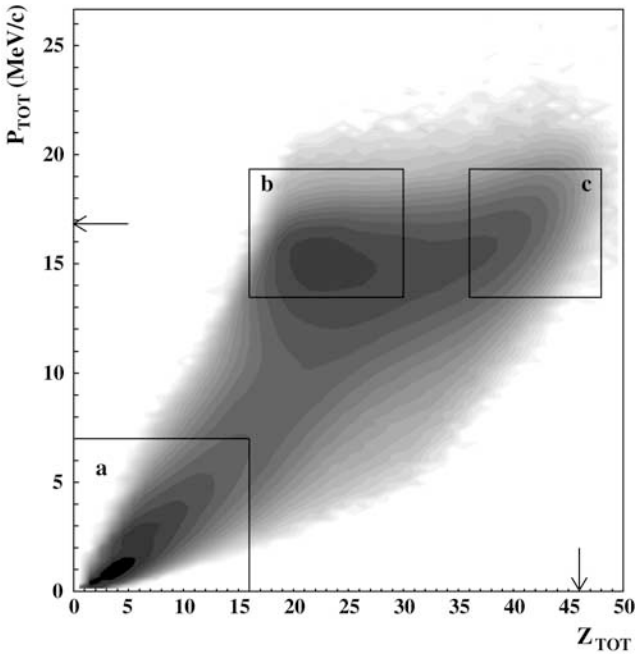

Fig. 7. Total linear momentum P_{tot} *versus* total charge Z_{tot} for all detected events from $^{36}\mathrm{Ar} + {}^{58}\mathrm{Ni}$ collisions at $95\,\mathrm{A}\cdot$ MeV. The arrows show the values of Z_{tot} and P_{tot} for the Ar + Ni system at $95\,\mathrm{A}\cdot$ MeV.

which are fully independent of the numerical technique (t_{clus} plus the coalescence algorithm) used to construct asymptotic predictions directly comparable with data, we have not found any measurable sensitivity to the parameters of the mean field. On the other hand, the mid-rapidity region of our system is strongly correlated with the value of the in-medium nucleon-nucleon elastic cross-section. Modifications of this parameter affect essentially the central and semi-central collisions, when the interaction zone between the two partners of the reaction in the first step of the collision is larger.

3 Experimental set-up and data selection

3.1 Experimental set-up

The 4π detection array INDRA was used at GANIL to investigate the reaction $^{36}\mathrm{Ar} + {}^{58}\mathrm{Ni}$ at $95\,\mathrm{A}\cdot$ MeV. A detailed description of INDRA can be found in refs. [37–39]. INDRA can be schematically described as an ensemble of 336 telescopes, which are distributed among 17 rings, covering 90% of the 4π solid angle. The most forward ring ($2^\circ \leq \theta \leq 3^\circ$), which may sustain a high flux of elastically scattered particles is made of phoswich detectors (NE102(0.5 mm) + NE115(25 cm)). From 3° to 45°, due to the required large energy dynamics, rings 2 to 9 are made of 180 three-stage telescopes (ionization chamber (5 cm of C_3F_8 at 50 mbar), Silicon (300 μm) and CsI (13.8 to 9 cm) deep enough to stop all particles). The angular range from 45° to 176° is covered by rings 10 to 17 made of 144 two-stage telescopes (ionization chambers (5 cm of C_3F_8 at 30 mbar) and CsI (7.6 to 5 cm)). For this experiment the ionization chambers were not installed for $\theta_{\mathrm{lab}} > 90^\circ$. In the forward region ($\theta < 45^\circ$), all ions are identified if their energies are greater than that corresponding to the Bragg peak. Beyond 45°, a clean identification is obtained up to $Z = 16$. An isotopic separation is also possible for $Z = 1$ to 4 in the last layer (CsI).

^{36}Ar beams produced by the GANIL facility were used to bombard a 193 $\mu\mathrm{g/cm}^2$ thick self-supporting ^{58}Ni target. The beam intensity was maintained around $3\text{–}4\times10^7$ pps to make negligible the rate of piled-up events. A multiplicity trigger was chosen, events were registered when at least four telescopes had fired.

3.2 Primary selection of the events

An overview of all events detected is shown in fig. 7, which presents the total detected momentum P_{tot} of identified particles as a function of the total detected charge Z_{tot}. The bidimensional plot can be divided in three regions which reflect the response of the detector.

- Region a): this region, corresponding to the low Z_{tot} and low P_{tot}, is associated with peripheral reactions, both the projectile-like and the target-like fragments remain undetected because of the energy threshold (target-like) and angular efficiency (projectile-like) effects.
- Region b): as soon as the projectile-like fragment is measured, the detected momentum P_{tot} comes close to

the projectile one. In this region, we can assume that the missing mass and the missing momentum are associated with only one fragment (the target-like residue).
– Region c): "well-detected" events are located in this region where more than 80% of the total charge and momentum were collected.

A global visualization of many-body events can only be accomplished if a maximum of information is collected on an event-by-event basis. In this aim, only "quasi-complete" events will be considered in this paper, namely those located in region c) in fig. 7.

3.3 Impact parameter selection

The aim of the paper is to obtain information on the nuclear interaction by comparing calculated and measured charge density distributions for different centrality bins. Indeed, the inclusive data cannot be directly compared to the total prediction of BNV which would be obtained by summing up all impact parameters, because the experimental impact parameter distribution is deformed. We thus have to find a global variable which can be used to select centrality in both the model and the experimental data. The correlation between the chosen variable and this experimental impact parameter, $b_{\rm exp}$, relies on a geometrical hypothesis [40]. A measure of the total reaction cross-section is needed to obtain a correct scale. For the complete data set of fig. 7, due to the on-line trigger (multiplicity ≥ 4), the total measured cross-section, calculated from the target thickness and the total number of incident ions, amounts to $\sim 70\%$ of the reaction cross-section calculated with the formula of Kox *et al.* [41]. The missing part corresponds to the most peripheral collisions.

An impact parameter selection through global variables presents some conceptual problems because of the unavoidable correlations with the charge density. In the INDRA experiments, a good impact parameter selector appears to be the light-particle transverse energy [7,8]. Indeed, INDRA has a high efficiency (about 90%) for light-charged-particle detection, independently of the reaction mechanism involved and of the impact parameter. Therefore, in this paper the experimental impact parameter, $b_{\rm exp}$, was determined from the transverse energy of light charged particles. Figure 8 represents the experimental correlation between the light-particle transverse-energy distribution and the impact parameter. For peripheral and mid-peripheral collisions ($E_{\rm trans12} \leq 0.6\ E_{\rm trans}^{\rm max}$) the correlation between $E_{\rm trans12}$ and $b_{\rm exp}$ is roughly linear. For more central collisions the correlation is weaker and one should not expect to discriminate between different violences of collision for $b_{\rm exp} < 0.3 \times b_{\rm max}$ ($b_{\rm max}$ is defined from the reaction cross-section [41]: $\sigma_{\rm R} = \pi b_{\rm max}^2$). In the event samples issued from the BNV calculation an "experimental" impact parameter $b_{\rm exp}$ was calculated as explained above with an absolute normalisation to the total reaction cross-section and it was verified that the impact parameter selection does not depend on $t_{\rm clus}$. The validity of $E_{\rm trans12}$ as a centrality selector is confirmed by the correlation between $b_{\rm exp}$ and the true impact parameter $b_{\rm theo}$ in BNV, shown in the lower part of fig. 8. The values of the "experimental" impact parameter were calculated with the standard parameters ($K = 220$ MeV and $\sigma_{N\text{-}N} = \sigma_{\rm free}$). For impact parameters between 2 and 7 fm, the $b_{\rm exp}$ distribution is centered on the true value of the impact parameter and the spread is relatively small. We can reasonably expect that the same spread should be present in the experimental data since the average $E_{\rm trans12}/b_{\rm exp}$ correlation and its width are comparable between experimental and simulated events (fig. 8, upper part).

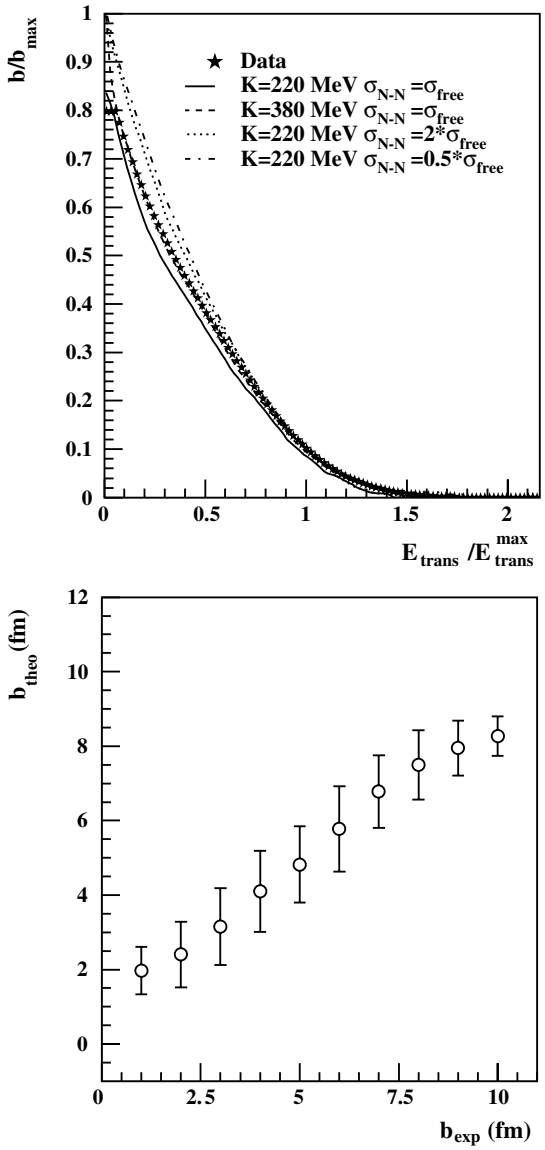

Fig. 8. Upper panel: correlation between the impact parameter $b_{\rm exp}$ and the light-particle (charge 1 and 2) transverse energy $E_{\rm trans12}$, normalized to a maximum value, corresponding to 1% of the reaction cross-section, for data and four different simulations. Lower panel: correlation between $b_{\rm exp}$ and $b_{\rm theo}$ for BNV events. The error bars correspond to the standard deviation of the "experimental" impact parameter distributions.

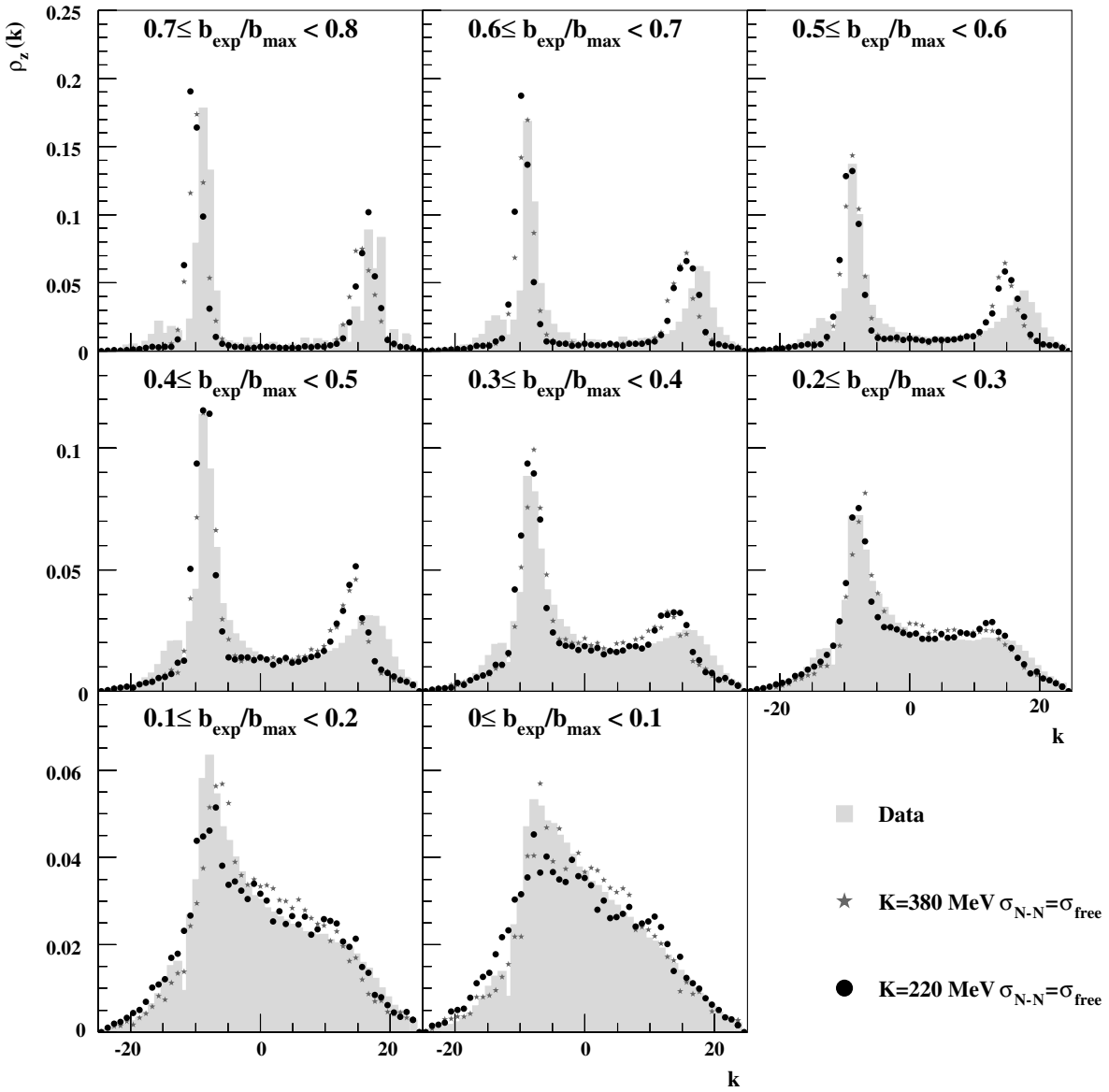

Fig. 9. Charge density distributions from $95\,\mathrm{A}\cdot$ MeV $^{36}\mathrm{Ar} + {}^{58}\mathrm{Ni}$ collisions for eight $b_{\mathrm{exp}}/b_{\mathrm{max}}$ bins, from $b_{\mathrm{exp}}/b_{\mathrm{max}} = 0.8$ to $b_{\mathrm{exp}}/b_{\mathrm{max}} = 0$; grey histograms represent experimental data and symbols refer to BNV simulations (black circles, $K = 220$ MeV and stars, $K = 380$ MeV). $k = V_{\mathrm{cm}}/12$.

4 Comparison between experimental and calculated charge density distributions

The event selection used (region c) in fig. 7) for all next results corresponds to about 10% of all recorded events with multiplicity ≥ 4, covers all classes of events. The absolute number of peripheral collisions in the selected sample is obviously low. It was verified that the samples for these collisions were not biased: within a given impact parameter class, observables from region c) in fig. 7 and from an enlarged region where only $Z_{\mathrm{tot}} \geq Z_{\mathrm{proj}}$ is required, agree in the forward momentum hemisphere. Keeping only region c) permits to study both the projectile and target velocity regions, furnishing thus complete information.

From the results of sect. 2, we expect that the charge density can provide information about the relative importance of the mean field and of the residual interaction in the nuclear interaction around $100\,\mathrm{A}\cdot$ MeV. The charge density was calculated for several $b_{\mathrm{exp}}/b_{\mathrm{max}}$ bins, for the experimental data and for BNV predictions with different sets of parameters of the nuclear interaction. The results are presented in figs. 9 and 10.

Experimental data are represented with light-grey histograms. The reactions evolve from an almost pure binary mechanism for semi-peripheral collisions ($b_{\mathrm{exp}}/b_{\mathrm{max}} < 0.8$) to collisions where a growing part of matter is found at mid-rapidity when the centrality increases [9,8]. The binary character remains, however, clearly dominant for all

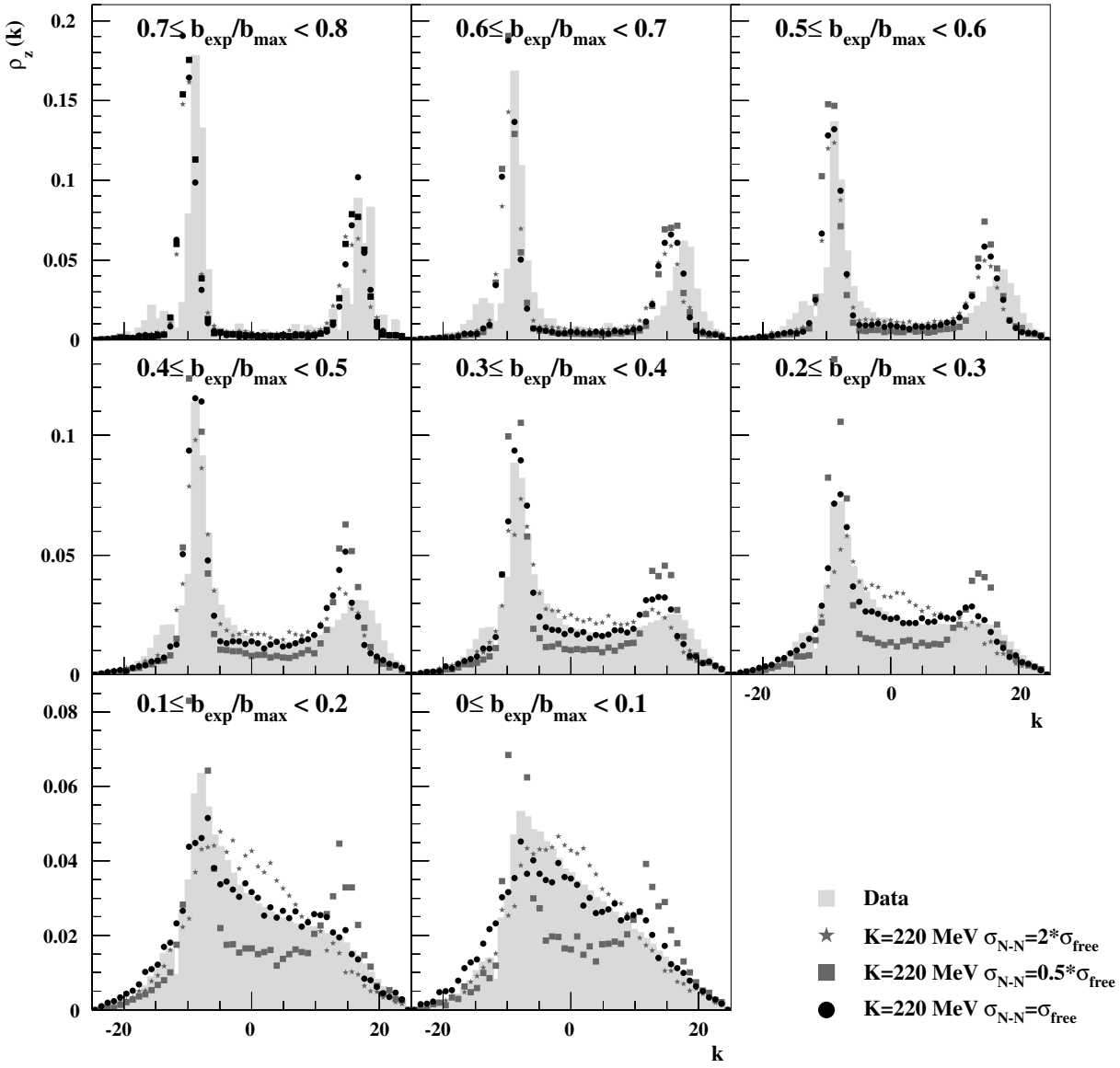

Fig. 10. Charge density distributions from $95\,\mathrm{A}\cdot\mathrm{MeV}$ $^{36}\mathrm{Ar} + {}^{58}\mathrm{Ni}$ collisions for eight $b_{\mathrm{exp}}/b_{\mathrm{max}}$ bins, from $b_{\mathrm{exp}}/b_{\mathrm{max}} = 0.8$ to $b_{\mathrm{exp}}/b_{\mathrm{max}} = 0$; grey histograms represent experimental data and symbols (circles, squares and stars) refer to BNV simulations for three values of the nucleon-nucleon cross-section. $k = V_{\mathrm{cm}}/12$.

collisions but perhaps the very central. The quasi-target seems to retain its identity even for rather central collisions while the peak of charges corresponding to the quasi-projectile stretches and tends to a plateau between the projectile and the center-of-mass velocities. The relative velocity between the quasi-projectile and the quasi-target shows almost no dependence on the collision centrality down to $b_{\mathrm{exp}}/b_{\mathrm{max}} = 0.3$. This result looks different from low-energy results related to the Deep Inelastic Process. A possible explanation is that a participant-spectator process better explains the reaction mechanism for the $^{36}\mathrm{Ar} + {}^{58}\mathrm{Ni}$ system at $95\,\mathrm{A}\cdot\mathrm{MeV}$. For the smaller impact parameter bin the two peaks are barely visible, which suggests a rather strong stopping.

BNV events, obtained with the standard set of parameters ($K = 220$ MeV and $\sigma_{N\text{-}N} = \sigma_{\mathrm{free}}$), are represented by the black circles in fig. 9. A first remark is that BNV well reproduces the general trend of the data. The relative velocity between the quasi-projectile and the quasi-target is slightly smaller in BNV, particularly at intermediate impact parameter, which would indicate too much dissipation. The position of the quasi-target peak may however suffer from detection biases (thresholds), but the effect is already visible on the quasi-projectile side alone. This effect is independent of the incompressibility coefficient but this does not exclude that data may show some sensitivity on the momentum dependence of the nuclear mean field. Studies in this direction are in progress. The lack of

sensitivity to the compressibility coefficient already seen in fig. 5 confirms that one-body dissipation is not very important in this reaction, similar to a participant-spectator scenario.

Let us turn now to the influence of $\sigma_{N\text{-}N}$, depicted in fig. 10. The data are still the light-grey histograms and BNV predictions are shown with grey stars, dark-grey squares and black dots. Clearly, setting $\sigma_{N\text{-}N} = 0.5 \times \sigma_{\text{free}}$ leads to a strong disagreement with the experimental data for all types of collisions. There is not enough stopping and a large transparency consistently appears for central collisions. This confirms the well-known fact that fusion in this energy regime is mostly due to two-body dissipation [42–44].

The best value of $\sigma_{N\text{-}N}$ for a matching with data lies between one and two times σ_{free}. This would provide the correct balance between the amount of mid-rapidity emission and the charge lying in the peak accumulated at the quasi-projectile velocity. The close similarity between the calculations at $\sigma_{N\text{-}N} = \sigma_{\text{free}}$ and $\sigma_{N\text{-}N} = 2 \times \sigma_{\text{free}}$ indicates that BNV simulations are already nearly at the limit of a hydrodynamic regime when the collision term is implemented with the free nucleon-nucleon cross-section. Note that again, whatever is the value of $\sigma_{N\text{-}N}$, the velocity of the quasi-projectile is slightly smaller in BNV than in experiment. This effect is thus independent of both the incompressibility coefficient and the nucleon-nucleon cross-section.

To summarize this part, a global comparison of experimental events with semi-classical dynamical simulations, *without attempting source separation*, appears very fruitful to get information on the nuclear interaction; the charge density is a powerful variable to fulfill this task. While the incident energy, $95\,\text{A} \cdot \text{MeV}$, is probably too high for allowing constraining studies of the mean-field part of the interaction, the experimental charge density distributions plead for a strong-collision term. This observation is in agreement with some of the published results on the expected medium effects on the nucleon-nucleon cross-sections [25,26].

5 The mid-rapidity component

It was demonstrated in the previous sections that the mid-rapidity part of the charge density distribution is the most sensitive probe of the nuclear interaction. In this section, further investigation on this emission will be attempted. Firstly, is it possible, with the help of the variable $\rho_z(k)$ to isolate and quantify the particles emitted during the nuclear-interaction stage? And secondly, which of the two incident partners, in the asymmetric system under study, populates the mid-rapidity component? Obviously, in the absence of strong isospin difference between the projectile and the target, only a theoretical answer can be given here to the second question.

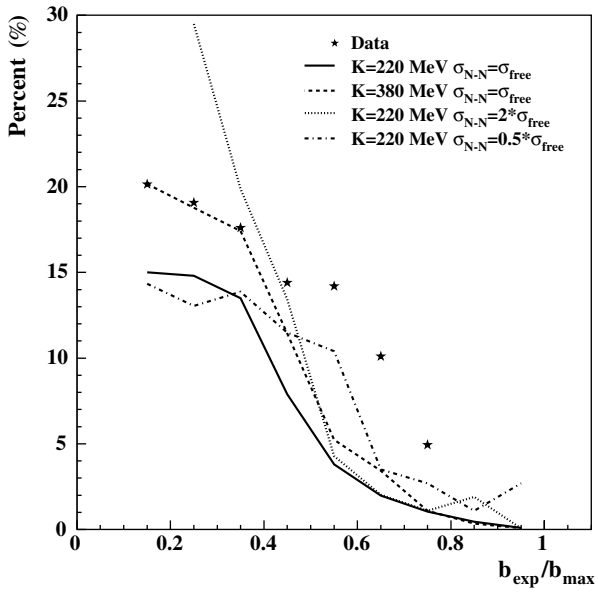

Fig. 11. Total percentage of the mid-rapidity component with respect to the total charge of the system as a function of $b_{\text{exp}}/b_{\text{max}}$, for experimental data (stars) and BNV simulations (lines) with different nuclear-interaction parameters.

5.1 Quantification of mid-rapidity charges

In the same spirit as in refs. [9–11] we can try a quantification of the mid-rapidity component viewed as the excess yield compared to an isotropic forward-backward emission from the quasi-projectile and the quasi-target sources. To this aim, for each centrality bin we have symmetrized the left (right) tail of the quasi-target (quasi-projectile) peak in the charge density distribution to simulate evaporation from the two spectators. The residual charge density, after subtraction of these peaks, is attributed to mid-rapidity emission, directly related to the nuclear-interaction process. Note that besides a severe hypothesis on the complete equilibrium (thermal and shape) of the final partners, it is implicitly assumed that the direct particle velocities are not too high and thus do not reach the very forward and very backward zones.

This procedure was applied to the experimental data and to the simulated events, for all $b_{\text{exp}}/b_{\text{max}}$ bins where the binary character in the exit channel is visible, thus excluding the most central ones. The evolution with the impact parameter of mid-rapidity charges (expressed as their percentage with respect to the total system charge) is displayed in fig. 11. The stars correspond to the experimental data and the lines show the values obtained from the BNV simulations for different couples $(K, \sigma_{N\text{-}N})$. As expected from the previous works, fig. 11 shows that the experimental percentage of mid-rapidity charges increases with centrality, up to 20% for the most central collisions. Although a similar evolution is obtained in the simulations, the model does not quantitatively reproduce the data, independently of the parameters of the interaction. This result seems incorrect and is misleading when compared to the conclusions of the previous sections derived from

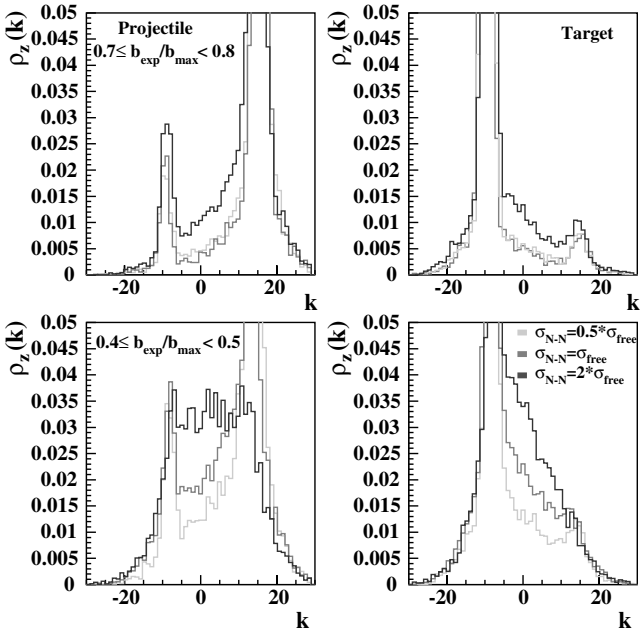

Fig. 12. BNV particle origin for different values of $\sigma_{N\text{-}N}$. K is always equal to 220 MeV. The charge density *versus* k indicates particles coming from projectile (left panels) and from target (right panels) for two $b_{\rm exp}/b_{\rm max}$ bins examples.

considering the charge density distribution in its globality (figs. 9 and 10). The apparent deviation shown by fig. 11 is due to the systematic shift of the quasi-projectile velocity peak between data and simulations. While this effect certainly shows that something in the BNV mean field is not properly treated, as discussed in the previous section, it has nothing to do with the quantity of charges emitted between the two peaks.

The results of figure 11 show that the quantification of mid-rapidity is subject to strong uncertainties and more generally that an analysis in terms of "emission sources" can be very dangerous for reactions where the two partners of the reaction are very close in momentum space. On the other hand, these ambiguities are absent if the reaction is analyzed globally as we have done in sect. 4.

5.2 First chance versus nuclear fireball

In the framework of the BNV model, it was shown in sect. 4 that the mid-rapidity emission seems to be associated to the residual interaction, namely to incoherent nucleon-nucleon elastic scattering. The question then naturally arises whether this phenomenon can be classified as first-chance nucleon-nucleon collisions or rather as the precursor of a nuclear fireball (multiple nuclear scattering). A way of answering this question for the BNV model consists in labeling the origin of the nucleons (projectile or target) and calculating the partial charge densities in different centrality bins.

The results are presented in fig. 12. The right panels correspond to the target contribution and the left panels to the projectile contribution. Only the soft equation of state was considered, with the three values of $\sigma_{N\text{-}N}$ used previously. Two examples of collisions are plotted: peripheral collisions in the upper panels and more central collisions in the lower panels. The mass transfer increases with the centrality of the collision as expected from the longer collision time. For the two partners (peaks of the charge density) the mass transfer is preferentially directed from the (lighter) projectile to the (heavier) target, in agreement with observations of low-energy deep inelastic collisions, while full relaxation is not reached [43]. The degree of mixing evolves from about 10% for peripheral collisions to about 30% for central collisions. Such a low percentage of exchanges justifies the low degree of relaxation of the incoming momentum observed in fig. 5 and fig. 9. The mid-rapidity region is populated by 60% of target nucleons and 40% of projectile nucleons, which corresponds to the target/projectile mass ratio. The result is the same for central and peripheral collisions and for the three different values of $\sigma_{N\text{-}N}$. This suggests that first-chance collisions cannot account for the mid-rapidity emission and rather plead for a multiple-scattering process.

6 Conclusion

Global variables allow an overall study of events resulting from heavy-ion collisions as well as of events built from semi-classical dynamical simulations. This avoids any arbitrary division of the reaction products in independent sources. A major application is therefore a direct comparison between experimental data and calculations in order to bring constraints on the nuclear interaction used in the models. In particular, charge density provides a direct visualization of the balance of charge between the mid-rapidity and the projectile/target regions of velocity. For the system studied in this paper, $^{36}\mathrm{Ar} + {}^{58}\mathrm{Ni}$ at $95\,\mathrm{A}\cdot\mathrm{MeV}$, this balance was shown to depend only slightly on the mean-field part of the interaction, and to be conversely very sensitive to the residual-interaction part, namely the influence of the nuclear medium on the nucleon-nucleon cross-section. The trend shown in this paper is consistent for all types of collisions, independently of their violence: the in-medium nucleon-nucleon cross-section needed to match the data is comparable to, or higher than, the free nucleon-nucleon cross-section.

We have shown that it is difficult to constrain the model parameters only from a three-source analysis from which the mid-rapidity contribution was extracted; it is better to perform a global analysis as we did in this paper.

Finally, a specific study of mass transfer between the incident nuclei in the framework of BNV indicates that mid-rapidity emission cannot be associated to first-chance nucleon-nucleon collisions but rather needs a higher degree of stopping; this result suggests a reaction mechanism close to a participant-spectator scenario for this reaction.

In order to get quantitative results on the in-medium effects of the nucleon-nucleon cross-section, as well as on the isospin and momentum dependence of the mean field, the protocol introduced in this paper has to be extended to a wider range of energies and isospin ratios.

References

1. B. Borderie, M. Montoya, M.F. Rivet, D. Jouan, C. Cabot *et al.*, Phys. Lett. B **205**, 26 (1988).
2. B. Lott, S.P. Baldwin, B.M. Szabo, B.M. Quedneau, W.U. Schröder *et al.*, Phys. Rev. Lett. **68**, 3141 (1992).
3. J.F. Lecolley, L. Stugge, M. Aboufirassi, A. Badala, B. Bilwes *et al.*, Phys. Lett. B **325**, 317 (1994).
4. INDRA Collaboration (V. Métivier, B. Tamain, G. Auger, C.O. Bacri, J. Benlliure *et al.*), Nucl. Phys. A **672**, 357 (2000).
5. M. Lefort, C. Ngô, Ann. Phys. (Paris) **3**, 5 (1978).
6. W.U. Schröder, J.R. Huizenga, *Treatise on Heavy Ion Science*, Vol. **2** (Plenum Press, New York, 1984).
7. INDRA Collaboration (J. Łukasik, J. Benlliure, V. Métivier, E. Plagnol, B. Tamain *et al.*), Phys. Rev. C **55**, 1906 (1997).
8. INDRA Collaboration (E. Plagnol, J. Łukasik, G. Auger, C.O. Bacri, N. Bellaize *et al.*), Phys. Rev. C **61**, 014606 (1999).
9. INDRA Collaboration (T. Lefort, D. Doré, D. Cussol, Y. Ma, J. Péter *et al.*), Nucl. Phys. A **662**, 397 (2000).
10. INDRA Collaboration (D. Doré, P. Buchet, J.L. Charvet, R. Dayras, L. Nalpas *et al.*), Phys. Lett. B **491**, 15 (2000).
11. INDRA Collaboration (P. Pawłowski, B. Borderie, G. Auger, C.O. Bacri, N. Bellaize *et al.*), Eur. Phys. J. A **9**, 371 (2000).
12. INDRA Collaboration (D. Doré, C. Volant, J. Cugnon, R. Legrain, G. Auger *et al.*), Phys. Rev. C **63**, 034612 (2001).
13. A. Bonasera *et al.*, Phys. Rep. **243**, 1 (1994).
14. F. Sébille, G. Royer, C. Grégoire, B. Remaud, P. Schuck, Nucl. Phys. A **501**, 137 (1989).
15. A. Guarnera, M. Colonna, P. Chomaz, Phys. Lett. B **373**, 267 (1996).
16. J. Aichelin, Phys. Rep. **202**, 233 (1991).
17. A. Ono *et al.*, Prog. Theor. Phys. **87**, 1185 (1992).
18. H. Feldmeier, Nucl. Phys. A **515**, 147 (1990).
19. INDRA Collaboration (J.F. Lecolley, E. Galichet, D.C.R. Guinet, R. Bougault, F. Gulminelli *et al.*), Nucl. Instrum. Methods Phys. Res. A **441**, 517 (2000).
20. K. Chen, Z. Fraenkel, G. Friedlander, J.R. Grover, J.M. Miller *et al.*, Phys. Rev. **166**, 949 (1968).
21. V. Greco, A. Guarnera, M. Colonna, M. Di Toro, Phys. Rev. C **59**, 810 (1998).
22. J. Singh, S. Kumar, R.K. Puri, Phys. Rev. C **62**, 044617 (2000).
23. G.Q. Li, R. Machleidt, Phys. Rev. C **48**, 1702 (1993).
24. G.Q. Li, R. Machleidt, Phys. Rev. C **49**, 566 (1994).
25. T. Alm, G. Röpke, M. Schmidt, Phys. Rev. C **50**, 31 (1994).
26. G. Giansiracusa, U. Lombardo, N. Sandulescu, Phys. Rev. C **53**, 1478 (1996).
27. C. Fuchs, L. Sehn, H. Wolter, Nucl. Phys. A **601**, 505 (1996).
28. V. Baran, M. Colonna, M. Di Toro, V. Greco, M. Zielinska-Pfabé *et al.*, Nucl. Phys. A **703**, 603 (2002).
29. M. Zielinska-Pfabé, C. Grégoire, Phys. Rev. C **37**, 2594 (1988).
30. E. Galichet, thèse de doctorat, Université Claude Bernard Lyon 1 (1998), LYCEN-T 9868.
31. INDRA Collaboration (J.D. Frankland, C.O. Bacri, B. Borderie, M.F. Rivet, M. Squalli *et al.*), Nucl. Phys. A **689**, 905 (2001).
32. INDRA Collaboration (M.F. Rivet, A. Chbihi, B. Borderie, D. Doré, P. Eudes *et al.*), Phys. Lett. B **388**, 219 (1996).
33. INDRA Collaboration (B. Borderie, D. Durand, F. Gulminelli, M. Pârlog, M.F. Rivet *et al.*, Phys. Lett. B **388**, 224 (1996).
34. E. Galichet, the INDRA Collaboration, in *Proceedings of the XXXVI International Winter Meeting on Nuclear Physics, Bormio, Italy (1998)*, edited by I. Iori (Università degli Studi di Milano).
35. M. D'Agostino, A. Botvina, M. Bruno, A. Bonasera, J.P. Bondorf *et al.*, Nucl. Phys. A **650**, 329 (1999).
36. INDRA Collaboration (N. Marie, R. Laforest, R. Bougault, J.P. Wieleczko, D. Durand *et al.*), Phys. Lett. B **391**, 15 (1997).
37. J. Pouthas, B. Borderie, R. Dayras, E. Plagnol, M.F. Rivet *et al.*, Nucl. Instrum. Methods Phys. Res. A **357**, 418 (1995).
38. J. Pouthas, A. Bertaut, B. Borderie, P. Bourgault, B. Cahan *et al.*, Nucl. Instrum. Methods Phys. Res. A **369**, 222 (1996).
39. J.C. Steckmeyer, D. Cussol, J. Duchon, J. Gautier, J. Laville *et al.*, Nucl. Instrum. Methods Phys. Res. A **361**, 472 (1995).
40. C. Cavata, M. Demoulins, J. Gosset, M.C. Lemaire, D. L'Hote *et al.*, Phys. Rev. C **42**, 1760 (1990).
41. S. Kox, A. Gamp, R. Cherkaoui, A.J. Cole, N. Longequeue *et al.*, Nucl. Phys. A **420**, 162 (1984).
42. B. Remaud, C. Grégoire, F. Sébille, L. Vinet, Phys. Lett. B **180**, 198 (1986).
43. B. Borderie, M.F. Rivet, L. Tassan-Got, Ann. Phys. (Paris) **15**, 287 (1990).
44. H.M. Xu, W.G. Lynch, P. Danielewicz, G.F. Bertsch, Phys. Rev. Lett **65**, 843 (1990).